Fibers and Polymers 2022, Vol.23, No.10, 2725-2731
DOI 10.1007/s12221-022-0175-6

ISSN 1229-9197 (print version)
ISSN 1875-0052 (electronic version)

Experimental and Simulation Investigation on the Effect of Slot Angle on the Flush Sharp Die Performance during Melt Blowing

Xibo Hao[1], Guojun Jiang[2,3,4], Jin Tao[1], Guoliang Liu[1], and Sheng Xie[2,3]*

[1]*School of Textile Garment and Design, Changshu Institute of Technology, Changshu 215500, China*
[2]*Key Laboratory of Yarn Materials Forming and Composite Processing Technology of Zhejiang Province, Jiaxing University, Jiaxing 314001, China*
[3]*Nanotechnology Research Institute, Jiaxing University, Jiaxing 314001, China*
[4]*Zhijiang College, Zhejiang University of Technology, Shaoxing 312000, China*
(Received March 1, 2022; Revised May 10, 2022; Accepted May 16, 2022)

Abstract: Die configuration is one of the most important factors that determine the polymer jet attenuation during melt blowing. To find the optimum slot angle, we investigated the effects of sharp die slot angles (60 °, 50 °, 40 °) on the polymer jet attenuation experimentally and numerically. A model which incorporated the air-polymer coupling effect was built based on phase field method to investigate the die performance. In the experiment, sharp dies with different slot angles were fabricated and adopted for producing melt-blown nonwovens. The SEM and filter efficiency measurement, and numerical analysis demonstrated that the 60 ° sharp die has the best performance in polymer jet attenuation.

Keywords: Melt blowing, Air-slot angle, Fiber attenuation, Numerical simulation, Experimental verification

Introduction

Melt blowing is a versatile and environmental benign method used in industry to produce micro-fibrous nonwovens. During melt blowing, fibers are produced in a single step by extruding polymer melt through an orifice die and attenuating the extrudate with converging high-speed and high-temperature air jets, as shown in Figure 1(a). The filament streams are captured by a collector positioned a distance away from the die, resulting in the formation of a nonwoven web with an almost random network of fibers [1-3]. The melt-blown products find applications in many areas such as filtration [4,5], oil sorbents [6,7], bone tissue engineering [8], and battery separators [9]. It is known that the performance of melt-blown nonwovens is highly related to its ultrafine fiber diameter [10]. Therefore, decreasing the fiber diameter would increase the property of the melt-blown nonwovens directly.

The process of melt blowing technology is complex [11,12], in which there are many different variables having impact on the final product. Experimental results from previous studies have established the facts that the average fiber diameter of melt blown nonwovens is mainly controlled by the melt throughput rate, melt viscosity, melt temperature, air temperature, and air velocity [2]. In addition, the die geometry also has great influence on the average fiber diameter of final product. The modifications of die configuration could be divided into two categories: modification of the die itself and using add-on devices to the existing die [13,14].

The slot angle is one of the most important geometry parameters that determine the performance of the slot die which is the most widely used die configuration. Tate and Shambaugh [15] measured the air flow field velocity of the die with slot angle of 60 ° and 70 °. They found that the flow field of a sharp 60 ° die has a higher maximum velocity than that of a sharp 70 ° die. With the help of CFD (computational fluid dynamics) technique, Krutka *et al*. investigated the effect of changing the angle (45 °, 50 °, 60 °, 70 °) on the flow field [16]. They believed that 45 ° slot angle is the best option for fiber attenuation for both blunt die and sharp die. In these two studies, the criterion for best slot angle is based on the centerline velocity and the premise that higher air velocity leads to higher drag on the polymer attenuation. Xie *et al*. [17] investigated the effect of lateral air velocity on fiber whipping. However, the influence of fiber on the flow field is also neglected. Moreover, the die performance should be determined by the final product, and this is absent in these previous studies. Our previous work [18] employed a phase-field method which incorporated the interplay between the fiber and air flow field to investigate the effect of slot angles on the performance of a blunt die. We found that the blunt dies with slot angle of 50 ° and 45 ° both show the highest fiber velocity than other angles (55 °, 60 °, 65 °, 70 °). However, the flaw of their conclusion lies in the lack of support of experiment.

From what has been discussed above, it could be concluded that the combination of experimental and theoretical work to investigate the effect of slot angle on fiber attenuation is rarely reported. The objective persued in this work is to adopt experimental and numerical methods to find the optimum slot angle for the attenuation of melt blown fibers. A type of sharp die with different slot angles were fabricated and adopted to produce melt blown fibers.

*Corresponding author: xie@zjxu.edu.cn

Numerical model was built based on the phase-field method to simulate the coupling effect between the fiber and air flow field, and the model was solved by Comsol Multiphysics. The optimum slot angle will be determined based on the experimental and numerical analysis.

Experimental

Materials and Device

A laboratory-scale melt-blowing device was employed to conduct experiments. The die installed in the melt-blown device has the configuration shown in Figure 1. The polymer resin provided by Hangzhou Chenda new material Co., Ltd. was 800-melt-flow-rate polypropylene with dynamic viscosity of 12 Pa·s at temperature of 240 °C. The die adopted is a flush sharp die, the configuration of which is depicted in Figure 1(b)-(c). The geometry parameters of which are listed in Table 1.

During the experiments, the processing parameters were air flow rates of 30 slm (1.67×10^{-5} m^3/min), a polymer flow rate of 1.2 cm^3/min, a polymer temperature of 240 °C, and an air temperature of 240 °C.

Characterization

The microstructure of the melt-blown nonwovens were conducted by a Phenom Pure scanning electron microscopy (Phenom Scientific, Netherlands). For each sample, about seven different places were scanned and captured into images. The fiber diameter was carried out by importing the electron microscopy image into Photoshop CS5 (Adobe, USA) and measuring the fiber diameter with the ruler tool. More than 20 fiber diameters were measured in each electron microscopy image, and fiber diameters were totally measured more than 150 times for each sample. Fiber mean diameter and standard deviation could be calculated by processing these discrete diameter data.

In addition, the fiber diameter of the melt-blown nonwoven was further analyzed by indirect indicators, i.e., filter efficiency (η) and filter resistance (ΔP). The η and ΔP nonwovens produced by the dies with different air-slot angles were measured by an type ZFT-2626-III filter efficiency tester (Wenzhou Fangyuan Instrucment Co., Ltd.). Due to the single spinneret could not produce nonwoven with width more than 13 cm, which was the minimum width requirement of samples for filter measurement. Therefore, a lateral reciprocator was made and carried the collected roller into an alternate lateral motion with speed of 0.01 m/s, meanwhile, the collected roller ran with linear velocity of 0.47 m/s (as shown in Figure 2(a)). Finally, a piece of nonwoven with width of 23 cm and length of 47 cm was obtained from the collected roller (Figure 2(b)). In the process of measuring the η and ΔP, the sodium chloride aerosols were used as tracing particles, and the air volume flow rate were 20 L/min, 32 L/min, and 85 L/min. Note that, all the nonwovens obatined in this work had fiber diameter larger than 10 μm, which was larger than the commerical melt-blown nonwovens [1], in order to increase the precision during the measurement, each obtained melt-blown nonwoven samples were measured by combining a standard melt-blown sample, i.e., one layer was the experimental nonwoven fabric and one layer was the standard nonwoven. The standard melt-blown sample had gram weight of 19 g/m^2 and had average fiber diameter of less than 3 μm, which was produced by a 1.2 m width industrial melt-blown equipment of Jiaxing University. The η and ΔP of the standard sample and the two layers (standard sample and the experimental sample) were measured respectively, the differences of η and ΔP could indicate the fiber properties of the experimental

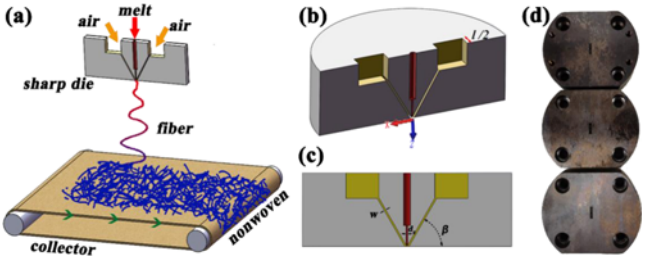

Figure 1. (a) Schematic of the melt blowing process, (b) oblique view of half of the die, (c) section view of the die, and (d) bottom vie of the dies fabricated.

Table 1. Geometry parameters of the sharp die

Geometry parameter	Value
Slot angle (β)	60 °, 50 °, 40 °
Slot length (l)	7 mm
Orifice diameter (d_0)	0.5 mm
Slot width (w)	0.5 mm

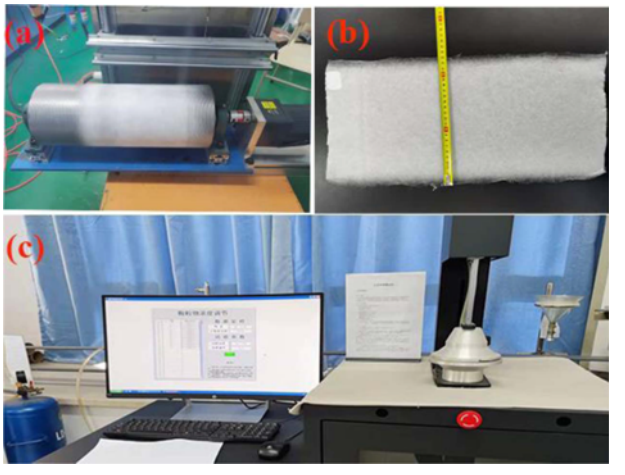

Figure 2. (a) Melt-blown nonwoven was collected by a roller and lateral areciprocator, (b) a piece of melt-blown nonwoven was obtained from the roller, and (c) the filter efficiency tester.

nonwovens of the present work.

Numerical Simulation

The phase-field method, based on a diffuse-interface description, is one of the most powerful approaches for modeling the microstructure evolution processes. The interfaces between domains are identified by a continuous variation of the properties within a narrow region [19]. In the Phase Field method, a Cahn-Hilliard equation is employed to track the fluid interface separating the immiscible phases (air and polymer). Here, the fluid interface is defined by the dimensionless phase field variable (Φ) which ranges between -1 and 1 continuously. The Cahn-Hilliard equation is decomposed into two equations (1), (2):

$$\frac{\partial Ø}{\partial t} + \mathbf{u} \cdot \nabla Ø = \nabla \cdot \frac{\gamma\lambda}{\varepsilon^2} \nabla \Psi \tag{1}$$

$$\Psi = -\nabla \cdot \varepsilon^2 \nabla Ø + (Ø^2 - 1)Ø \tag{2}$$

where, **u** refers to the fluid velocity (m/s), t denotes time for the fluid motion (s), γ is the mobility (m^3s/kg), λ is the measure of mixing energy density (N) and ε is interface thickness (m). Equation (3) establishes a relationship between the interface thickness, mixing energy density and the surface tension coefficient (σ) which is set to be 0.02 N/m [20].

$$\lambda = \frac{3\varepsilon\sigma}{2\sqrt{2}} \tag{3}$$

The interface thickness parameter is related to the characteristic mesh size (h_c) in the region passed by the interface by equation (4).

$$\varepsilon = \frac{h_c}{2} \tag{4}$$

The time scale required by the Cahn-Hilliard diffusion is determined by the mobility parameter. The mobility parameter must be large enough to retain a constant interfacial thickness, while small enough to ensure that the convective terms are not overly damped. The mobility parameter is a function of the interface thickness, as described in equation (5).

$$\gamma = \chi\varepsilon^2 \tag{5}$$

where, χ is a constant and controls the mobility of the interface. Here, it is set to be 1.

In the present model, the volume faction of polymer jet and air in the computational area is defined by equation (6), and equation (7), respectively.

$$V_{f1} = \frac{1 - Ø}{2} \tag{6}$$

$$V_{f2} = \frac{1 + Ø}{2} \tag{7}$$

The density (kg/m^3) and the viscosity (Pa·s) of the mixture varying smoothly over the interface are defined by equation (8) and equation (9), respectively.

$$\rho = \rho_{air} + (\rho_{poly} - \rho_{air})V_{f2} \tag{8}$$

$$\mu = \mu_{air} + (\mu_{poly} - \mu_{air})V_{f2} \tag{9}$$

where parameters ρ, ρ_{air} and ρ_{poly} are density of the air-polymer two phase flow, air flow and polymer jet, respectively. The parameters μ, μ_{air}, μ_{pol} are dynamic viscosity of the air-polymer two phase flow, air flow and polymer jet, respectively. Here, ρ_{air}, ρ_{poly}, μ_{air} and μ_{pol} are set to be 1.293 kg/m^3, 900 kg/m^3.

The conservation of momentum and mass are described in equation (10) and equation (11), respectively.

$$\rho\frac{\partial \mathbf{u}}{\partial t} + \rho(\mathbf{u} \cdot \nabla)\mathbf{u} = -\nabla p + \nabla \cdot [(\mu + \mu_T)(\nabla \mathbf{u} + (\nabla \mathbf{u})^T)] + F_{st} + \rho g \tag{10}$$

$$\frac{\partial \rho}{\partial t} + \nabla \cdot (\rho \mathbf{u}) = 0 \tag{11}$$

where μ_T is the turbulence viscosity, p is pressure of the fluid, F_{st} is the surface tension force acting at the air/polymer interface, g is gravity acceleration. The surface tension force can be deduced from equation (12).

$$F_{st} = \frac{\lambda}{\varepsilon^2} \Psi \nabla Ø \tag{12}$$

It is a widely acknowledged fact that flow filed during melt blowing is turbulent. The common turbulence model k-ω is applied to describe the turbulent flow. The k-ω model for the transport of kinetic energy is as follows:

$$\rho\frac{\partial k}{\partial t} + \rho(\mathbf{u} \cdot \nabla)k = \nabla \cdot [(\mu + \mu_T \sigma_k^*)\nabla k] + P_k - \beta_0^* \rho \omega k \tag{13}$$

In addition to the kinetic energy transport equations, the dissipation rate is modeled by the following equation:

$$\rho\frac{\partial \omega}{\partial t} + \rho(\mathbf{u} \cdot \nabla)\omega = \nabla \cdot [(\mu + \mu_T \sigma_\omega^*)\nabla \omega] + \alpha\frac{\omega}{k} P_k - \rho\beta_0 \omega^2 \tag{14}$$

where, k is turbulence kinetic energy, ω is specific dissipation rate, P_k is production term. The turbulence model parameters $\alpha, \sigma_k^*, \sigma_\omega, \beta_0, \beta_0^*$ are set to be 0.52, 0.5, 0.5, 0.072, 0.09, respectively.

Figure 3 depicts the computational domain and boundary conditions for the sharp-die air flow. The origin of the computational domain locates at the center of the die face, with the x-direction traversing the major slot axis; the z-direction is in the downward direction below the die and perpendicular to the die face; the y-axis (not shown) is

perpendicular to the two-dimensional plane of the computational domain. The dimensions of rectangular area in the computational domain are 40 mm in the x-direction and 60 mm in the *z*-directions. As shown in Figure 3, the inlet for air flow entering the computational domain (black boundaries) was defined as a velocity inlet of air. The left, right and the bottom boundaries (blue boundaries) were all set as pressure outlets with ambient pressure of 0 Pa. The inlet where polymer flow entering the computational domain (green boundary) was defined as a velocity inlet of polymer. The exit for polymer where the polymer meet air, was defined as an initial interface (purple boundary). The other boundaries including the wall of the polymer channel, the wall of air channel and die face are defined as wall (red boundaries).

The grid is a combination of the structured and unstructured elements, as depicted in Figure 4. Computational domain in the rectangular area under the die was discretized into quadrilateral elements, while in the other area was discretized into triangular elements. The grid resolution of the area where polymer jet goes through is fine structured. To find

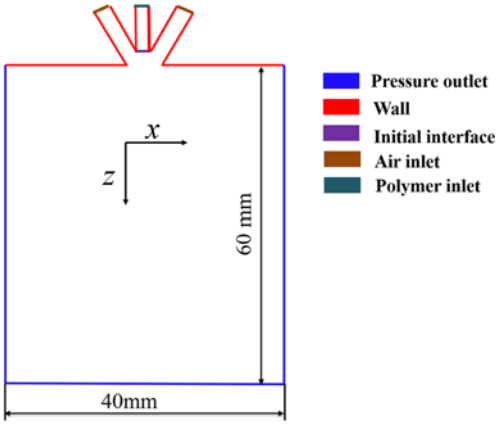

Figure 3. Computation domain and boundary conditions for the sharp-die airflow.

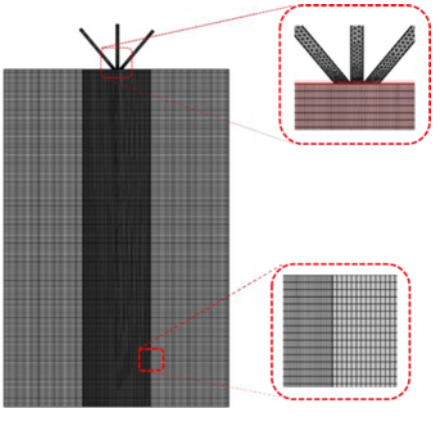

Figure 4. Mesh for the computation domain.

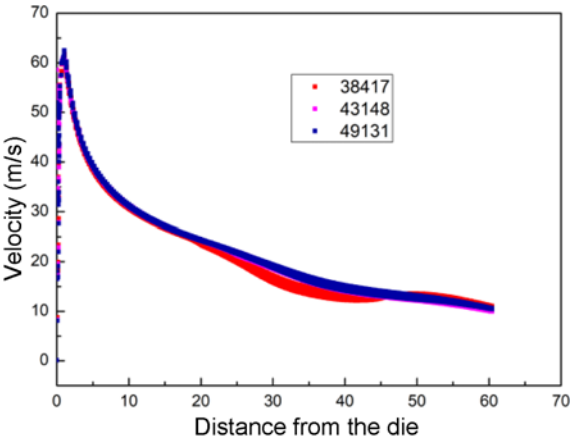

Figure 5. Grid independence test for the computational domain of Die A.

the optimum mesh density, the computation domains were meshed into 38417, 43148 and 49131 elements, respectively. Figure 5 depicts distribution of polymer jet velocity calculated with different mesh density. It is observed that the curve of 43148 elements is in the same pattern with that of 49131 elements, while different with that of the 38417 elements. Thus, the mesh with 43148 elements is the optimum option.

Results and Discussion

Polymer Jet Motion of Different Dies

Figure 6 depicts the fiber motion and the velocity distribution of the polymer jet produced by 60 ° sharp die at different times. It is discovered that polymer jet is unstable, and according to the theory of Yarin *et al.* [11], the instability of the melt-blown polymer jet is induced by the turbulent nature of the high speed gas. The instability could be seen in two aspects: the trajectory and velocity distribution of the polymer jet. The initial section of the polymer jet is nearly straight and the whipping motion is seen at a further distance. Similar to the jet trajectory, for the velocity distribution at different times, there is no apparent difference in the initial section of the polymer jet. And the velocity difference lies in the section further from the die.

The data of the velocity distribution of polymer jet produced by dies with different slot angles at different times was plotted into scatter diagrams and exhibited in Figure 7(a)-(c). For each die, the polymer jet velocity is nearly same in the initial section and divergent at the position about 20 mm away from the die at different times. Figure 7(a)-(c) indicate that the diameter uniformity of melt-blown fibers might be caused by the divergence of polymer jet motion in the area further from the die. Figure 7(d)-(i) presents the effects of slot angles on polymer jet velocity at the times of 0.05 s, 0.06 s, 0.07 s, 0.08 s, 0.09 s and 0.1 s, respectively. It is observed that the die with slot angle of 60 ° has the highest

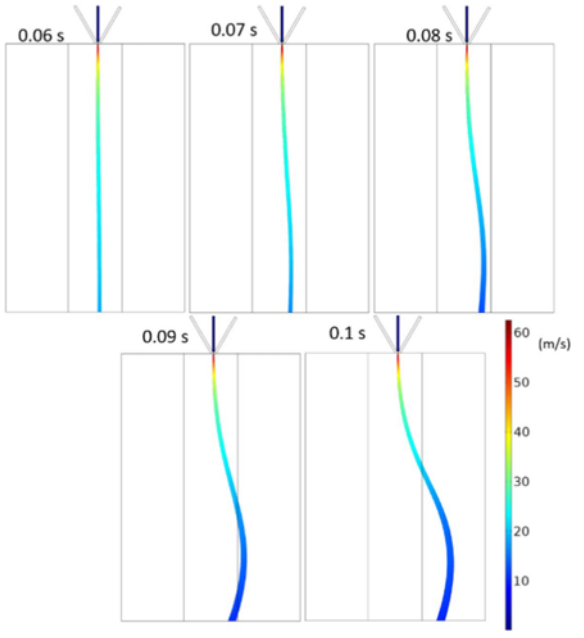

Figure 6. Configurations and velocity distributions of the polymer jet produced by Die A with slot angle of 60 ° at different times.

polymer jet velocity, followed by the sharp die with slot angle of 50 ° and 40 ° at any time. However, the gap between them is not obvious. From the aspect of air, with the increase of slot angle, air velocity in the *y* direction increases. It seems that, for the configuration of this sharp die, the increase of the air velocity in the y direction is beneficial for the polymer jet attenuation.

Fiber Diameter of Different Dies

Based on the polymer jet velocity predicted above and the continuity equation (equation (15)), we could make an estimation of the fiber diameter produced by dies with different slot angles.

$$\pi r^2 v \rho_f = W \tag{15}$$

In equation (15), r is the radius of polymer jet, ρ_f is density of the molten polymer, v is the polymer jet velocity, W is the mass flow rate of polymer. Here, W, ρ_f and π are constant. V could be acquired from the computation results.

The calculated fiber diameter is exhibited in Figure 8. The predicted diameters of fibers produced by the die with slot

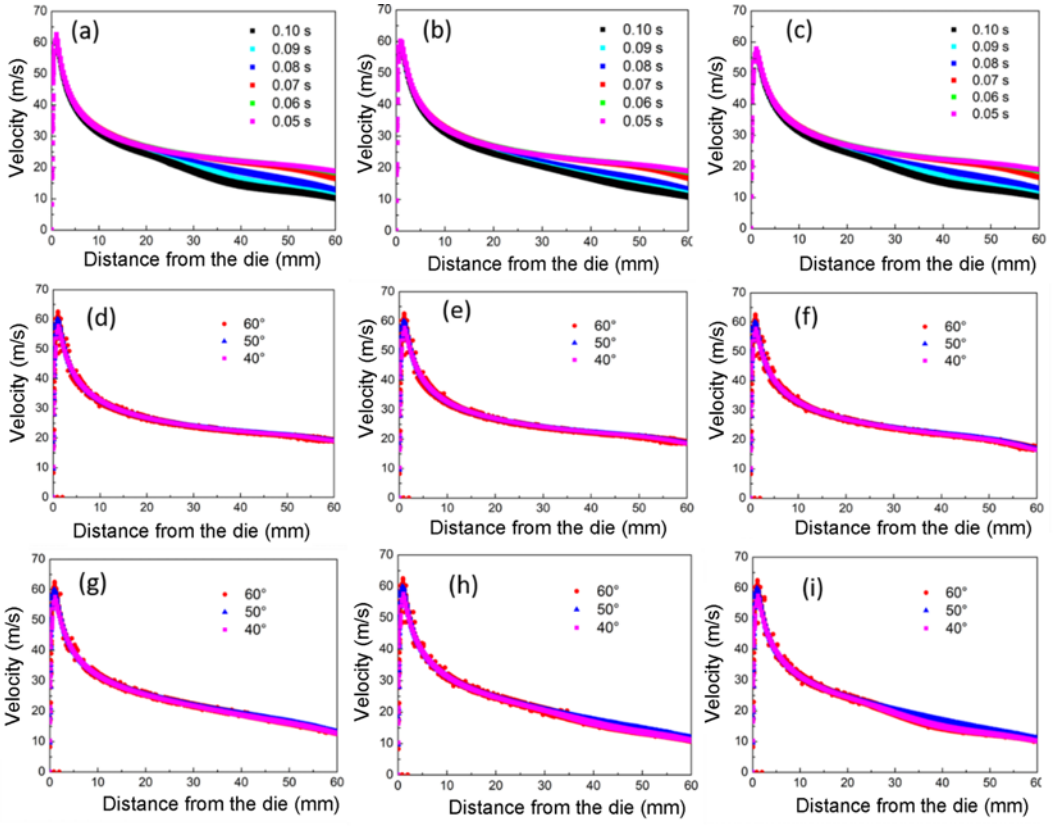

Figure 7. (a) Velocity distribution of the polymer jet produced by the sharp-die with slot angle of 60 ° at different times, (b) velocity distribution of the polymer jet produced by sharp-die with slot angle of 50 ° at different times, (c) velocity distribution of the polymer jet produced by sharp-die with slot angle of 40 ° at different times, and (d-i) velocity distribution of the polymer jet produced by sharp-die with different slot angles at the time of 0.05 s, 0.06 s, 0.07 s, 0.08 s, 0.09 s, 0.1 s, respectively.

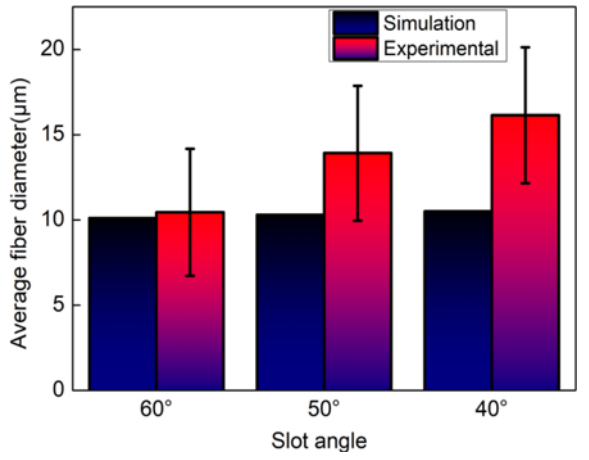

Figure 8. Comparison between the experimental and simulation fiber diameter produced by Die A.

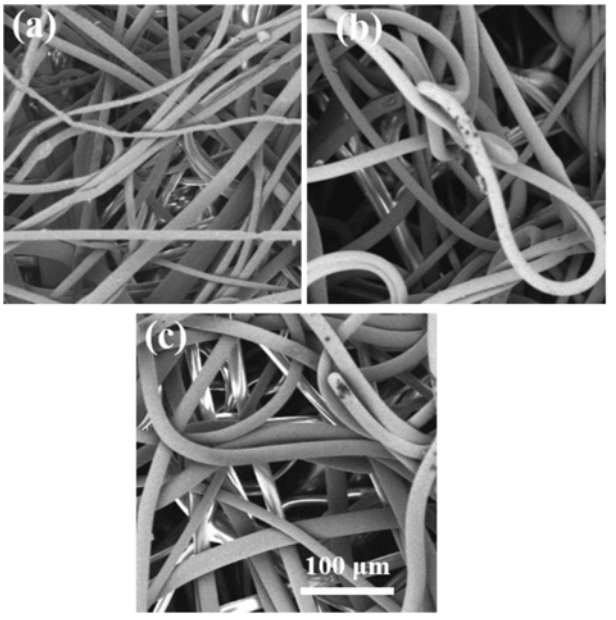

Figure 9. Scanning electron microscopy images of the fiber produced by the die with slot angle of (a) 60 °, (b) 50 °, and (c) 40 °.

angles of 60 °, 50 ° and 40 °, are 10.1 μm, 10.3 μm and 10.5 μm, respectively. The experimental value of the fiber diameter is also exhibited in Figure 8. The fiber diameter measurement result with slot angle of 60 °, 50 ° and 40 °, are 10.5 μm, 13.9 μm and 16.1 μm, respectively. The fiber diameter coefficient variation of the nonwovens produced by the die with slot angles of 60 °, 50 ° and 40 ° are 0.356, 0.284 and 0.247 μm, respectively. The numerical value is higher than the experimental value, which is due to the fact that the predicted diameter is based on the fiber velocity near the die. In fact, the fiber attenuation also happened in the other area. Besides, the model doesn't consider the three-dimensional motion of the polymer jet.

Table 2. Filter efficiency (η) and filter resistance (ΔP) of nonwovens

Kind of sample	Measured air volume (L/min)	η (%)	ΔP (pascal)
Standard sample	20	99.30	39
Standard+die 60 ° sample	20	99.67	54
Standard+die 50 ° sample	20	99.51	49
Standard+die 40 ° sample	20	99.50	39
Standard sample	32	98.60	60
Standard+die 60 ° sample	32	99.00	86
Standard+die 50 ° sample	32	98.80	69
Standard+die 40 ° sample	32	98.70	67
Standard sample	85	92.00	151
Standard+die 60 ° sample	85	96.70	209
Standard+die 50 ° sample	85	93.40	166
Standard+die 40 ° sample	85	93.00	158

The SEM images of fibers produced by different dies are shown in Figure 9. Both the measurement values and predicted values support the conclusion that the sharp die with slot angle of 60 ° has the highest polymer attenuation and the predicted values are close to the experimental values. In addition, the filter efficiency (η) and filter resistance (ΔP) of nonwovens are shown in Table 2, regardless of the inlet air volume condition, the melt-blown nonwoven obtained by the die with 60 ° air slot angle has higher filter efficiency (η) and corresponding higher filter resistance (ΔP) than that by die with 50 ° air slot angle, and the melt-blown nonwoven obtained by the die with 40 ° has the lowest filter efficiency (η) and filter resistance (ΔP). Table 2 reveals that the melt-blown sharp die with air slot angle of 60 ° can manufacture the finest fibers.

Conclusion

In this work, the effects of slot angles on the performance of sharp die were investigated by experimental and numerical methods. Sharp dies with different slot angles (60 °, 50 °, 40 °) were fabricated and employed for producing melt-blown nonwovens. SEM measurement indicated that 60 ° sharp die has the highest attenuation for polymer jet and the average fiber diameter gaps between the three groups are distinct. A phase field method was employed to establish an air-polymer coupled model for the prediction of attenuation of polymer jet extruded by different dies. The simulation results are consistent with the experimental observation.

Acknowledgement

This work is supported by the National Natural Science Foundation of China (11702113), the Jiaxing Project of

Science and Technology (2022AY10002), the Open Project Program of Key Laboratory of Yarn Materials Forming and Composite Processing Technology of Zhejiang Province (MTC-2022-02), the China Postdoctoral Science Foundation (2020M671594), and Natural Science Foundation of Colleges in Jiangsu Province (19KJB540002).

Conflict of Interest

The author(s) declared no potential conflicts of interest with respect to the research, author-ship, and/or publication of this article.

References

1. X. B. Hao and Y. C. Zeng, *Ind. Eng. Chem. Res*., **58**, 11624 (2019).
2. J. Drabek and M. Zatloukal, *Phys. Fluids*, **31**, 091301 (2019).
3. W. L. Han and X. H. Wang, *Fiber. Polym.*, **15**, 1190 (2014).
4. T. Jiang, G. Zeng, C. Hu, C. Meng, and Y. Chen, *Fiber. Polym*., **22**, 957 (2021).
5. X. Zhang, J. X. Liu, H. F. Zhang, J. Hou, Y. X. Wang, C. Deng, C. Huang, and X. Y. Jin, *Polymers*, **13**, 485 (2021) .
6. F. Sun, T. T. Li, H. T. Ren, Q. Jiang, H. K. Peng, Q. Lin, C. W. Lou, and J. H. Lin, *Polymers*, **11**, 775 (2019).
7. J. Zhao, C. F. Xiao, and N. K. Xu, *Environ. Sci. Pollut. Res.,* **20**, 4137 (2013).
8. W. H. Gazzola, R. S. Benson, and W. Carver, *Ann. Plast. Surg.*, **83**, 716 (2019).
9. H. Wang, Y. Zhang, H. P. Gao, X. Y. Jin, and X. H. Xie, *Int. J. Hydrogen Energy*, **41**, 324 (2016).
10. C. J. Ellison, A. Phatak, D. W. Giles, C. W. Macosko, and F. S. Bates, *Polymer*, **48**, 3306 (2007).
11. S. Sinha-Ray, A. L. Yarin, and B. Pourdeyhimi, *J. Appl. Phys.*, **108**, 034912 (2010).
12. S. Xie, G. J. Jiang, B. L. Ye, and B. Q. Shentu, *Polymers*, **12**, 279 (2020).
13. R. L. Shambaugh, J. D. Krutty, and S. M. Singleton, *Ind. Eng. Chem. Res.*, **54**, 12999 (2015).
14. S. F. Xin, X. H. Wang, and S. Z. Hu, *J. Text. Res*., **36**, 71 (2015).
15. A. S. Harpham and R. L. Shambaugh, *Ind. Eng. Chem. Res.*, **36**, 3937 (1997).
16. H. M. Krutka, R. L. Shambaugh, and D. V. Papavassiliou, *Ind. Eng. Chem. Res.*, **43**, 4199 (2004).
17. S. Xie, W. L. Han, X. F. Xu, G. J. Jiang, and B. Q. Shentu, *Polymers*, **11**, 788 (2019).
18. X. B. Hao, Z. Y. Zhao, and J. Wei, *J. Ind. Text*., doi.org/10.1177/15280837211006670 (2021).
19. Y. L. Li, S. Y. Hu, X. Sun, and M. Stan, *Npj Comput. Mater*., **1**, 333 (2017).
20. F. Boyer, C. Lapuerta, S. Minjeaud, B. Piar, and M. Quintard, *Trans Porous. Med*., **82**, 463 (2010).